



Article

Electron Absorbed Fractions and S Factors for Intermediate Size Target Volumes: Comparison of Analytic Calculations and Monte Carlo Simulations

Christina Kotroumpelou ¹, Ioanna Kyriakou ¹ , Vladimir Ivanchenko ², Sebastien Incerti ³ 
and Dimitris Emfietzoglou ^{1,*}

¹ Medical Physics Lab, Department of Medicine, University of Ioannina, 45110 Ioannina, Greece; x.kotroumpelou@gmail.com (C.K.); ikyriak@uoi.gr (I.K.)

² CERN, CH-1211 Geneva, Switzerland; vladimir.ivantchenko@cern.ch

³ University of Bordeaux, Centre National de la Recherche Scientifique, Laboratoire de Physique des Deux Infinis, Unité Mixte de Recherche 5797, F-33170 Gradignan, France; incerti@lp2ib.in2p3.fr

* Correspondence: demfietz@uoi.gr; Tel.: +30-2651007741

Abstract: The absorbed fraction and the S factor represent fundamental quantities in MIRD-based dosimetry of radiopharmaceutical therapy (RPT). Although Monte Carlo (MC) simulations represent the gold standard in RPT dosimetry, dose point kernels (DPK) obtained from analytic range–energy relations offer a more practical alternative for charged-particle dosimetry (β - or α -emitters). In this work, we perform DPK- and MC-based calculations of the self-absorbed fractions and S factors for monoenergetic electrons uniformly distributed in intermediate-size target volumes (~mm to cm) relevant to micrometastasis and disseminated disease. Specifically, the aim of the present work is as follows: (i) the development of an analytic range–energy relation, effective over a broad energy range (100 keV–20 MeV) covering most applications of radiotherapeutic interest; (ii) the application of the new formula to DPK-based calculations of the absorbed fraction and S factor and comparison against MC simulations (both published and present work data) as well as the MIRDcell V2.0.16 software, which uses a similar analytic methodology; and (iii) the study of the influence of simulation parameters (step-size, tracking/production cut-off energies, and ionization model) in Geant4-based calculations of S factors. It is shown that the present DPK-based calculations are in excellent agreement (within 1.5%) with the MIRDcell software, while also being in fair agreement with published MC data as well as with the new Geant4 simulations, with average differences of ~20% for the (sub) mm-sized volumes and ~10% for the cm-sized volumes. The effect of the choice of Geant4 simulation parameters was found to be negligible for the examined target volumes (~mm), except for the use of the Penelope ionization model, which may exhibit noticeable discrepancies (up to ~20%) against the Standard and Livermore models. The present work provides quantitative information that may be useful to both the MC- and DPK-based beta dosimetry of micrometastasis and disseminated disease, which represents an important field of application of RPT.

Keywords: absorbed fraction; S factor; internal dosimetry; electron dosimetry; Geant4



Citation: Kotroumpelou, C.; Kyriakou, I.; Ivanchenko, V.; Incerti, S.; Emfietzoglou, D. Electron Absorbed Fractions and S Factors for Intermediate Size Target Volumes: Comparison of Analytic Calculations and Monte Carlo Simulations. *Appl. Sci.* **2024**, *14*, 2275. <https://doi.org/10.3390/app14062275>

Academic Editor: Maria Filomena Botelho

Received: 19 January 2024

Revised: 28 February 2024

Accepted: 2 March 2024

Published: 8 March 2024



Copyright: © 2024 by the authors. Licensee MDPI, Basel, Switzerland. This article is an open access article distributed under the terms and conditions of the Creative Commons Attribution (CC BY) license (<https://creativecommons.org/licenses/by/4.0/>).

1. Introduction

The goal of radiation therapy is the delivery of a lethal radiation dose to cancer cells with minimum toxicity in surrounding healthy tissues. In recent years, radiopharmaceutical therapy (RPT) has been a promising method for the treatment of many cancer types [1]. In RPT, radiation is delivered to tumor cells and their microenvironment with the use of agents or through physiological mechanisms [2]. An important advantage of RPT is that, unlike external beam radiotherapy, the radiation can more effectively target disseminated and micrometastatic disease [3]. To that end, studies in the fields of radiobiology, radiochemistry, and pharmacology are important for selecting the proper combination of radionuclides

and chemical agents toward improving treatment outcomes [2]. The radionuclides that are used in RPT are mainly β -emitters (and less so α -emitters). The advantage of β -emitters is that the irradiation range is commonly in the mm–cm range and, therefore, to a good approximation, they result in a uniform dose distribution in the tumor volume even when the emitter is non-uniformly distributed, as is most often the case due to its limited diffusion. In addition, in sharp contrast to γ -emitters, the shorter irradiation range of β -emitters offers much greater sparing of surrounding healthy tissues raising the therapeutic index [3,4].

The response and the toxicity of any radiotherapeutic modality depend upon the absorbed dose to the tumor and the normal tissue. The standard approach for the calculation of absorbed dose in RPT follows the formalism provided by the Medical Internal Radiation Dose (MIRD) Committee of the American Society of Nuclear Medicine. The dosimetric formalism of the MIRD Committee was first presented in 1968 and since then a series of developments has been published in specialized publications (MIRD pamphlets) [5]. The central quantities in MIRD-based RPT dosimetry are the absorbed fraction and the S factor [1]. These quantities are determined by either Monte Carlo (MC) simulations or dose point kernels (DPKs). In turn, DPKs may be determined using either MC simulations or analytic techniques, such as range–energy relations. Information about absorbed fractions and S factors from the organ to the cellular scale for most radionuclides and monoenergetic photons or electrons is available in various MIRD publications [6–13].

At the macroscopic scale of organs and tissues, absorbed fractions and S factors are mostly calculated [12,14–16] by general-purpose MC codes, like ETRAN [17], EGS [18], MCNP [19], and Geant4 [20]. These codes are well benchmarked at the organ/tissue scale (~cm) and represent the gold standard in clinical dosimetry (both internal and external). At the other extreme of the (sub) cellular scale (<10 to 100 μ m), absorbed fractions and S factors are mostly determined [21–25] by specialized MC track-structure codes, like KURBUC [26], PARTRAC [27], and Geant4-DNA [28–31], among others reviewed in [32]. At the intermediate scale (sub-mm to cm), which includes disseminated and micrometastatic disease, both general-purpose and track-structure codes may be applied with each approach having its pros and cons. However, irrespective of the code, MC simulations are generally time-consuming and require substantial software expertise to avoid systematic errors or simulation artifacts. Therefore, to facilitate the practical application of the absorbed fraction and S factor in RPT dosimetry, DPK-based analytic approaches offer a valuable theoretical alternative to MC simulations by reducing computational time.

Using the ETRAN code, Berger first provided the energy deposition of photon point sources in water [33] and afterward, the distribution of the absorbed dose of point sources of electrons and beta-emitting particles in water and other media [34,35]. Siegel and Stabin [36] used Berger's works and developed an analytical formula to calculate the absorbed fraction of monoenergetic electrons (25 keV–4 MeV) and beta-emitters, which are uniformly distributed in unit density spheres of different sizes (0.13–6.20 cm). The Siegel–Stabin results have been used by Stabin and Konijnenberg for comparison with EGS4 and MCNP [37]. Later, Amato and co-workers [38] calculated the absorbed fractions for electrons uniformly distributed in ellipsoidal volumes by Geant4 version 9.1. In that study, the absorbed fractions in spheres for monoenergetic electrons were determined for comparison with the recommended values of Stabin and Konijnenberg [37]. These studies [37,38] are included in the more recent work of Olguin et al. [39], which presented the absorbed fraction and the S factor for targets of different sizes and compositions. Specific absorbed fractions were calculated by the MCNPX code for monoenergetic photons, electrons, and α -particles in spherical and ellipsoidal tumor volumes, while S factors for 22 radionuclides were also provided.

The aim of the present study is (i) the development of an analytic range–energy relation, effective over the energy range from 100 keV to 20 MeV, which covers most applications of radiotherapeutic interest; (ii) the use of the new formula for DPK-based calculations of the absorbed fraction and S factor and their comparison against MC simulations (both published and present work data) as well as the MIRDcell software that uses a

similar analytic methodology; and (iii) the study of the influence of simulation parameters (step-size, tracking/production cut-off energies, and ionization model) in Geant4-based calculations of S factors. The motivation for the development of a new analytic formula is to overcome the energy limitations of the existing formulas, thus facilitating the application of DPK-based analytic methods as an alternative to effort- and time-intensive MC simulations in the calculation of the absorbed fraction and S factor in RPT dosimetry. The work focuses on “intermediate” size target volumes (~mm to cm), relevant to micrometastasis and disseminated disease, which represent an important field of application of RPT. The validation of the present analytic formulas is limited to the energy range from 100 keV to 4 MeV, which covers the usage of β -emitters in RPT, and published data of the absorbed fraction and S factor are available. However, the proposed parameterization extends up to 20 MeV electron energies, in order to cover potential application to external beam radiotherapy (EBRT).

2. Materials and Methods

2.1. MIRD Range–Energy Relations

MIRD scheme [40] is a formalism for absorbed dose calculations of internally distributed radionuclides. The mean absorbed dose in target region r_k from source region r_h is given by the equation:

$$\bar{D}(r_k \leftarrow r_h) = \tilde{A}_h S(r_k \leftarrow r_h), \quad (1)$$

where \tilde{A}_h is the cumulated activity in the source region r_h and S is the mean absorbed dose in the target region per unit of cumulative activity in the source region. The S factor can be expressed as

$$S(r_k \leftarrow r_h) = \sum_i \frac{\Delta_i \varphi_i(r_k \leftarrow r_h)}{m_k}, \quad (2)$$

where φ_i is the absorbed fraction, which is the fraction of energy emitted in region r_h , and it is absorbed in region r_k ; Δ_i is the mean energy emitted per nuclear transition for the i -th type of emission; and m_k is the mass of the target. S factors are provided by MIRD Committee for most radionuclides, from organ level [9] to cellular level [41]. Also, S factors are available for monoenergetic photons [6,8,37] and electrons [34,36]. For microscopic dimensions (nm to mm) relevant to sub-cellular, cellular, and multi-cellular domains, MIRD adopts the continuous slowing down approximation (CSDA) to calculate S factors using analytic range–energy relations [41]. The CSDA assumes that the energy loss of the primary particle is “continuous” and neglects the finite range of secondary electrons (i.e., it assumes that the energy of secondary electrons is deposited at the point of their production). Then, for a uniformly distributed radiation source inside a spherical target, the absorbed fraction that enters Equation (2) may be calculated from the DPK using the following convolution integral [1]:

$$\varphi_i(r_k \leftarrow r_h) = \int \Psi_{r_k \leftarrow r_h}(r) F\left(\frac{r}{r_0}\right) d\left(\frac{r}{r_0}\right), \quad (3)$$

where $\Psi_{r_k \leftarrow r_h}$ is the geometric reduction factor and $F(r/r_0)$ is the (scaled dimensionless) DPK. The geometric factor is the mean probability that a randomly directed vector of length r that starts from a random point within the source region r_h ends within the target region r_k . For charged particles (e.g., β -emitters), Equation (3) may be recast in terms of the stopping power as follows [1]:

$$\varphi_i(r_k \leftarrow r_h) = \int \Psi_{r_k \leftarrow r_h}(r) \frac{1}{E_i} \frac{dE}{dR} \Big|_{R(E_i)-r} dr, \quad (4)$$

where E_i is the initial energy of the i -th particle, and $dE/dR|_{R(E_i)-r}$ is the energy-loss rate (i.e., similar to the stopping power) evaluated at $R(E_i)-r$, which is the residual range of a particle with initial energy E_i after passing a distance of r through the medium [41]. The MIRD Committee suggests [5] the use of Cole’s range–energy relations for determining

in Equation (4) the stopping power dE/dR and the residual range $R(E_i)-r$ [42]. Cole experimentally determined the range of electrons in some low-Z solid materials with energies from 20 eV to 100 keV, and deduced the following empirical relations [42]:

$$E(R) = 5.9(R + 0.007)^{0.565} - 0.367, \quad (5)$$

$$R(E) = 0.0431(E + 0.367)^{1.77} - 0.007, \quad (6)$$

where E is expressed in keV and R in μm . By differentiation of Equation (5), the following stopping power expression (in $\text{keV}/\mu\text{m}$) is obtained:

$$\frac{dE}{dR}(R) = 3.316(R + 0.007)^{-0.435}, \quad (7)$$

For electron energies extending from 100 keV up to 20 MeV, Cole suggested another set of expressions as follows [42]:

$$E(R) = 5.9(R + 0.007)^{0.565} + 0.00413R^{1.33} - 0.367, \quad (8)$$

$$\frac{dE}{dR}(R) = 3.333(R + 0.007)^{-0.435} + 0.0055R^{0.33}, \quad (9)$$

where E is expressed in keV and R in μm . Subsequently, Howell provided improved range–energy relations that better fit Cole’s experimental data for electron energies less than 0.4 keV [43]. The Cole–Howell expressions read (E in keV and R in μm):

For energies from 0 to 0.06 keV:

$$R(E) = a + bE + cE^2 + dE^3, \quad (10)$$

where $a = 1.524 \times 10^{-3}$, $b = 3.815 \times 10^{-2}$, $c = -7.018 \times 10^{-4}$, $d = 3.628 \times 10^{-2}$, and

$$\frac{dE}{dR} = 29.5 - 666.7R, \quad (11)$$

For energies from 0.06 to 0.4 keV:

$$R(E) = 0.0123E + 2.25E^2 - 23.33E^3, \quad (12)$$

$$\frac{dE}{dR} = a + bR + cR^2 + dR^3 + eR^4, \quad (13)$$

where $a = 10.5$, $b = 1.126 \times 10^3$, $c = -9.251 \times 10^5$, $d = 2.593 \times 10^8$, and $e = 4.964 \times 10^{10}$.

2.2. New Range–Energy Relations

As mentioned above, range–energy relations are needed to calculate, via the convolution integral of Equation (4), the absorbed fraction and subsequently the S factor by Equation (2). The calculation of the convolution integral is greatly facilitated by the availability of analytic expressions for both dE/dR and $R(E)$. The Cole–Howell relations for dE/dR and $R(E)$ conveniently cover the energy range up to 100 keV. However, for energies above 100 keV, Cole does not provide an analytic expression for $R(E)$, and, therefore, the residual range $R(E_i)-r$ has to be calculated numerically from $E(R)$. Therefore, to facilitate calculations of the absorbed fraction and S factor by the convolution integral of Equation (4), we have fitted the experimental range–energy data deduced from Equation (8). These new (fitted) range–energy relations are analytic and valid for monoenergetic electrons over the energy range 100 keV to 20 MeV, which covers the β -emitters used in RPT (<4 MeV) as well as most applications of electron beams in EBRT (up to ~ 20 MeV). The analytic form of this new set of range–energy relations, $R(E)$, is presented below (E in keV and R in μm).

For energies from 100 keV to 1 MeV:

$$R(E) = 1.281E^{0.7} - 1.534E^{1.33} + 1.042E^{1.5} - 0.06626E^{1.77} - 0.4652, \quad (14)$$

For energies from 1 MeV to 4 MeV:

$$R(E) = 2.167E^{0.7} + 0.4123E^{1.4} - 0.01055E^{1.77} - 60.93, \quad (15)$$

For energies from 4 MeV to 20 MeV:

$$R(E) = 4.910E^{1.05} - 0.1336E^{1.33} - 368.9, \quad (16)$$

These new set of expressions, Equations (14)–(16), may be combined with the Cole–Howell expressions, Equations (5)–(7) and (10)–(13), to calculate the absorbed fraction over a very broad energy range from 20 eV to 20 MeV.

2.3. MIRDcell Software

The MIRD Committee developed a software application, called MIRDcell (<http://mirdcell.njms.rutgers.edu/>, accessed on 18 January 2024), which calculates the distribution of radiation dose and predicts the surviving fraction of cell populations [44]. The user can select the size, shape, and geometry of the cell population, the distribution of radioactivity, and the source of radiation. The available sources of radiation are predefined MIRD radionuclides, monoenergetic particles, or a radionuclide created by the user. The continuous spectrum and the mean energy of β -emitters are also available options. The cellular model used in MIRDcell consists of two concentric homogeneous spheres of unit density. The external sphere represents the cell with radius R_C and the other one is the nucleus with radius R_N , respectively. The radioactivity is distributed in the source region of the cell, nucleus, cytoplasm, or cell surface [45]. The target region and the size of the radius of the cell and nucleus are selected by the user. The Software also includes a functionality that creates a cell population of any shape and of 2 or 3 dimensions, and calculates the dose distribution among the labeled cells. After the selection of these parameters, MIRDcell calculates the S factor of target region and the survival fraction based on the linear quadratic model. Importantly, MIRDcell calculates the S factor using the Cole–Howell analytic range–energy relations, Equations (5)–(7) and (10)–(13), for electron energies below 100 keV, and numerical data from Equations (8) and (9) for energies above 100 keV [41]. In the present work, for comparative purposes, (self-irradiation) S factors for monoenergetic electrons with initial energy 1 keV–4 MeV were calculated for cell spheres with different radii using the MIRDcell V2.0.16 version.

2.4. Geant4 Configuration

Geant4 [20,46–48] is a Monte Carlo toolkit for simulating the interaction of particles in matter. It has been used in different applications like high-energy physics, astrophysics and space science, medical physics, and radiation protection. For MeV electrons, Geant4 offers several condensed-history electromagnetic (EM) models to facilitate the simulation of a large number of interactions [49]. In particular, the Standard EM package is used for the simulation of interactions of particles with energy up to 10 PeV [47]. Also included are the Livermore and Penelope low-energy EM models [50], which are particularly effective at sub-1 keV energies. Both these models employ single-scattering cross sections to simulate the discrete energy losses in hard inelastic collisions, restricted stopping power for the continuous energy losses in soft inelastic collisions, and multiple scattering theories for the elastic collisions. The hard and the soft inelastic collisions are differentiated by the production cut-off energy (selected by the user), which defines the energy threshold above which the secondary particles are individually simulated [51]. The user also selects the tracking cut-off energy, which defines the energy below which primary and secondary

electrons are “killed”; i.e., when the energy of the particle falls below the tracking cut-off energy, the particle is no longer simulated, and its energy is deposited locally.

In this work, Geant4 version 10.5 is used, which is the same version used in the Geant4 validation for medical physics applications.

2.4.1. Geant4-Livermore

The Livermore EM model is based on the data libraries EPDL97 [52], EADL [53], and EEDL [54] and is appropriate for the simulation of photon and electron transport in materials with $Z = 1-100$. The hard collisions are described through the Möller cross-section model and the soft collisions using the Weizsacker–Williams expression. For the multiple elastic scattering, the Urban model is used [55]. The Livermore ionization model may be used for energies down to a few 10 eV, although an energy limit of 250 eV is often recommended for better accuracy. The Livermore model considers the shell structure of atomic elements but neglects condensed-phase effects, which may be important for sub-keV electron transport and microscopic volumes [56].

2.4.2. Geant4-Penelope

The Penelope EM model is derived from the PENELOPE code version 2008 [57] and is applicable to simulations of photons and electrons in materials with $Z = 1-100$. Inelastic collisions are described by the Generalized Oscillator Strength (GOS) model of Liljequist [58]. Multiple elastic scattering is simulated by the Urban model [55]. Note that the Geant4-Penelope models do not apply for energies lower than 100 eV and, similar to the Livermore models, neglect condensed-phase effects [56].

2.4.3. Geant4-Standard Option 4

The Standard Option 4 model of Geant4, version 10.5 [47], describes the inelastic collisions using the Livermore ionization model for electron energies lower than 100 keV and the Standard EM (default models) for higher energies. The interactions are differentiated into hard and soft collisions by the selection of production cut energy. The energy loss at hard collisions is calculated by sampling the differential cross sections. For soft collisions, the energy loss is treated as a continuous process, and stopping power expressions are used. The cross sections and the stopping power expressions for Livermore and Standard EM (default models) are presented in the following Table 1. Also, the Goudsmit–Saunderson model [59] is used for the multiple elastic scattering.

Table 1. Cross sections and stopping power expressions for Standard Option 4 model of Geant4.

Geant4		Standard Option 4	
e-Ionization model	Livermore model for electrons < 100 keV	soft collisions	Stopping power from Weizsacker–Williams cross section
		hard collisions	Weizsacker–Williams ionization cross section
	Standard model for electrons > 100 keV	soft collisions	Berger–Seltzer stopping power formula
		hard collisions	Möller ionization cross section
e-Multiple elastic scattering	Goudsmit–Saunderson model		

2.4.4. Geant4 Simulations

The simulations’ results are based on the *Svalue* example of Geant4 version 10.5. The absorbed fractions and S factors presented are based on a batch of 1 million histories (primary electron tracks). From several independent runs of each batch (of 1 million histories) for selected data points, the statistical uncertainty (one standard error) was

estimated to be below 1%. The primary electron energy in the simulations varied from 1 keV up to 4 MeV. The S factor is estimated for spheres with radius 100 μm ($R = 0.1$ mm), 1000 μm ($R = 1$ mm), and 5000 μm ($R = 5$ mm), which are relevant to micrometastasis and disseminated disease. The geometry of the simulation is presented schematically in Figure 1, where the external sphere (“world”) with radius R_W is the volume that encompasses the full slowing-down radiation tracks, and the internal sphere with radius R_T represents the source/target volume where the radiation source (here, the monoenergetic electrons) is randomly placed and energy deposition is recorded. It is important to mention that R_W is significantly greater than the CSDA range of electrons, so that all electrons (primary or secondary) stop within the world volume. The tracking and production cut-off energies examined are 100, 250, and 1000 eV. The first two values represent the recommended cut-off energies for the Penelope (100 eV) and Livermore (250 eV) models, whereas the latter value (1 keV) is characteristic of general-purpose class II condensed-history codes (e.g., EGS4). The Step Length (SL) values examined are $SL = \text{default}$, $SL = R$, and $SL = R/10$. The choice of the above transport parameters had a very small impact (up to a few %) on the simulation time (~ 0.3 s/track in an 8-core Intel i3-2130 @3.4 GHz Processor) with the exception of the Penelope model, which resulted in a reduction in simulation time by almost a factor of 10.

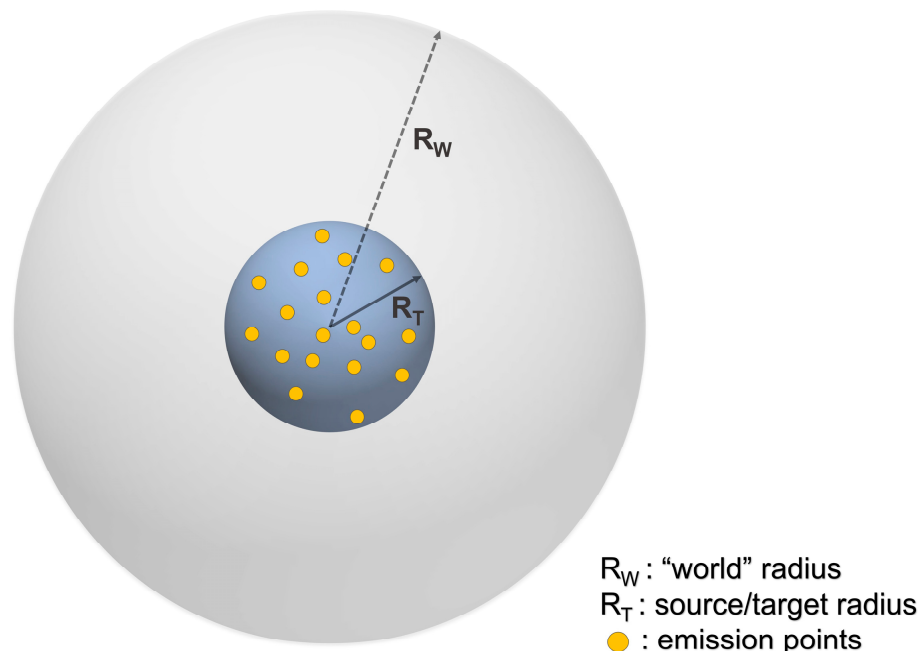


Figure 1. Simulation geometry. The external sphere represents the “world” volume with radius R_W , and the internal sphere represents the source/target volume with radius R_T .

3. Results

3.1. Range

The electron CSDA range (or average path length) in liquid water is calculated using Cole’s formula (Equation (6)) and the new analytic relations of the present work (Equations (14)–(16)). The results are shown in Figure 2, along with the most recent CSDA range data of ICRU Report 90 [60].

Figure 3 shows the percentage difference, $100 \frac{(R_{PW} - R_{Cole})}{R_{Cole}}$, between the calculations of the present work (PW) and Cole’s data for electron energies from 100 keV to 20 MeV, which is the application regime of the present formulas.

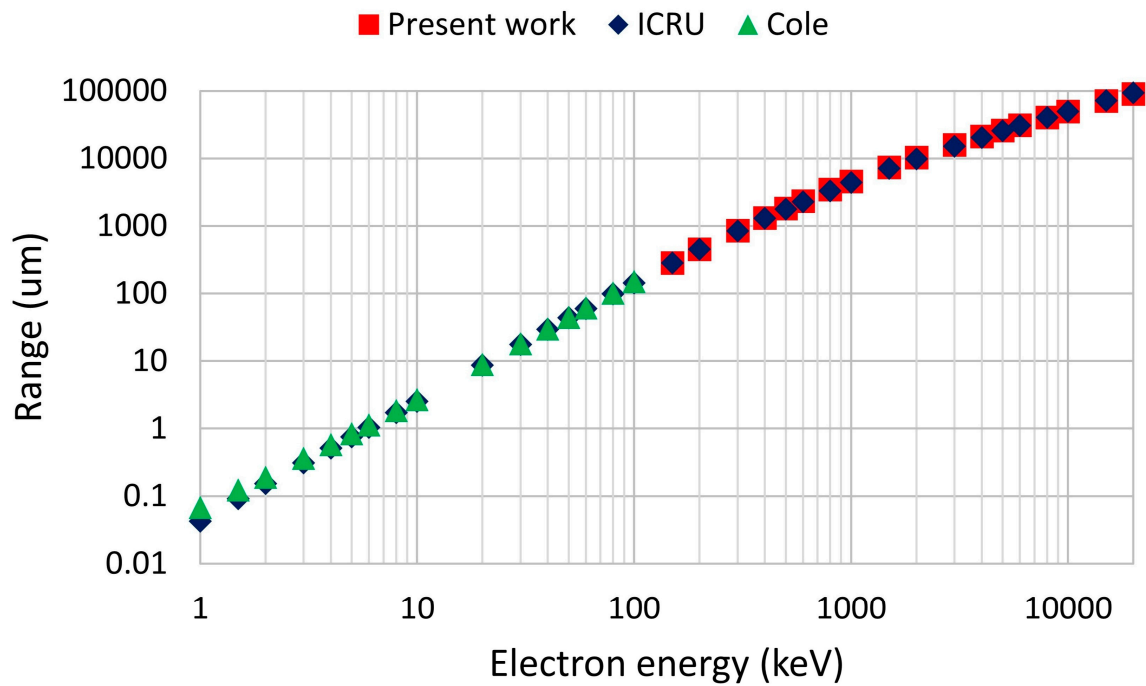


Figure 2. The CSDA range data as a function of electron energy. Boxes: present work; Triangles: Cole’s relation; Rhombus: data from ICRU Report 90.

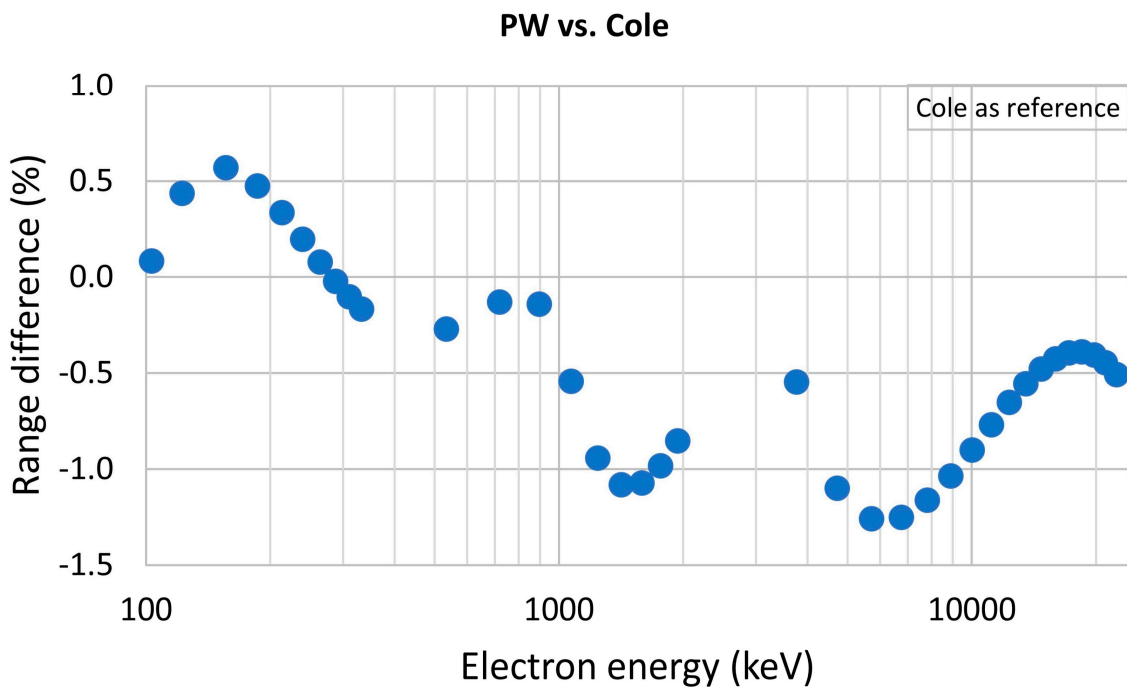


Figure 3. Percentage difference of electron CSDA range between the calculations of the present work (PW) and Cole’s data as a function of electron energy.

Figure 4 shows that the percentage difference, $100 \frac{(R_{PW} - R_{ICRU})}{R_{ICRU}}$, between the calculations of the present work (PW) and ICRU Report 90 over the 100 keV–20 MeV energy range, which is the application regime of the present formulas.

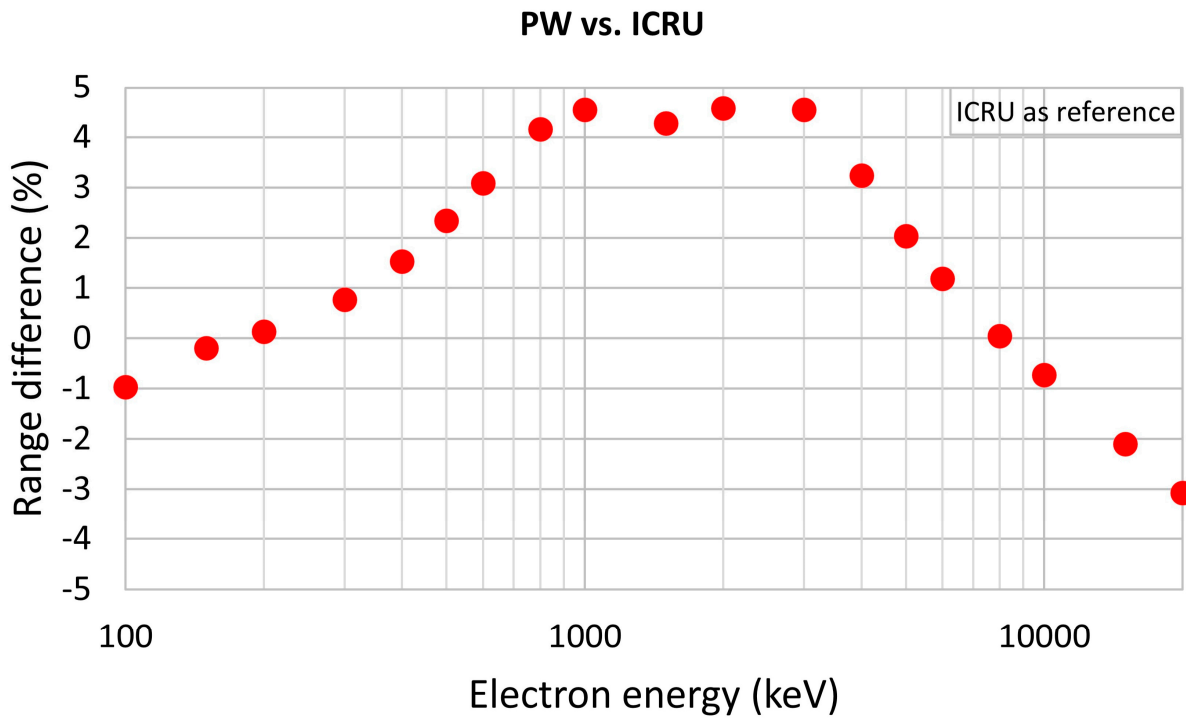


Figure 4. Percentage difference of electron CSDA range between the calculations of the present work (PW) and ICRU Report 90 as a function of electron energy.

3.2. Absorbed Fraction (AF) Calculations

Absorbed fractions (AF) for monoenergetic electrons distributed uniformly in unit-density spheres of different radii are calculated using the convolution integral, Equation (4), and the present analytic relations, Equations (14)–(16). The size of target spheres (radius 1.3 mm to 6.2 cm) was chosen in order to compare the present results against the available MC simulation data from the literature for electron energies in the range 100 keV–4 MeV. In Figure 5, the percentage difference, $100 \frac{(AF_{MC} - AF_{PW})}{AF_{PW}}$, between the MC data and the results of the present work (PW), is depicted for the various spheres and MC codes examined.

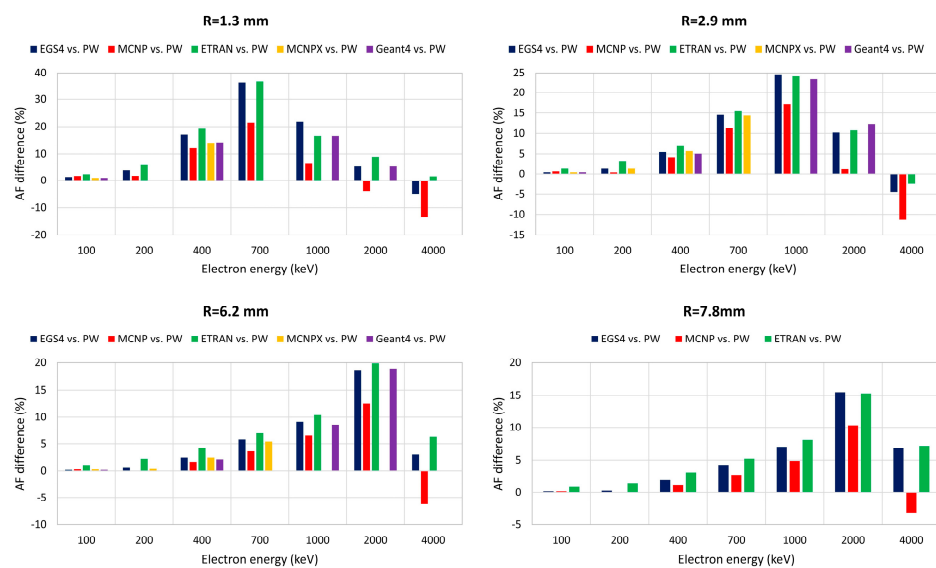


Figure 5. Cont.



Figure 5. Percentage difference of absorbed fraction (AF) between published MC simulation data from different codes (EGS4, MCNP, ETRAN, MCNPX, Geant4) and the analytic calculations of the present work (PW), for several electron energies in the range 100 keV–4 MeV and different sphere radii (1.3 mm–6.2 cm).

When averaged over the electron energies examined (E_i), the mean percentage (absolute) difference of the AFs, $100 \frac{1}{N} \sum_{i=1}^N \left| \frac{(AF_{MC,E_i} - AF_{PW,E_i})}{AF_{PW,E_i}} \right|$, and the maximum percentage (absolute) difference of the AFs, $\text{Max} \left\{ 100 \left| \frac{(AF_{MC,E_i} - AF_{PW,E_i})}{AF_{PW,E_i}} \right| \right\}$, between the MC data and the results of the present work (PW) for each sphere radius is depicted in Figure 6. To put these differences in perspective, the maximum and mean percentage differences between the MCNP and EGS4 codes are also included in Figure 6.

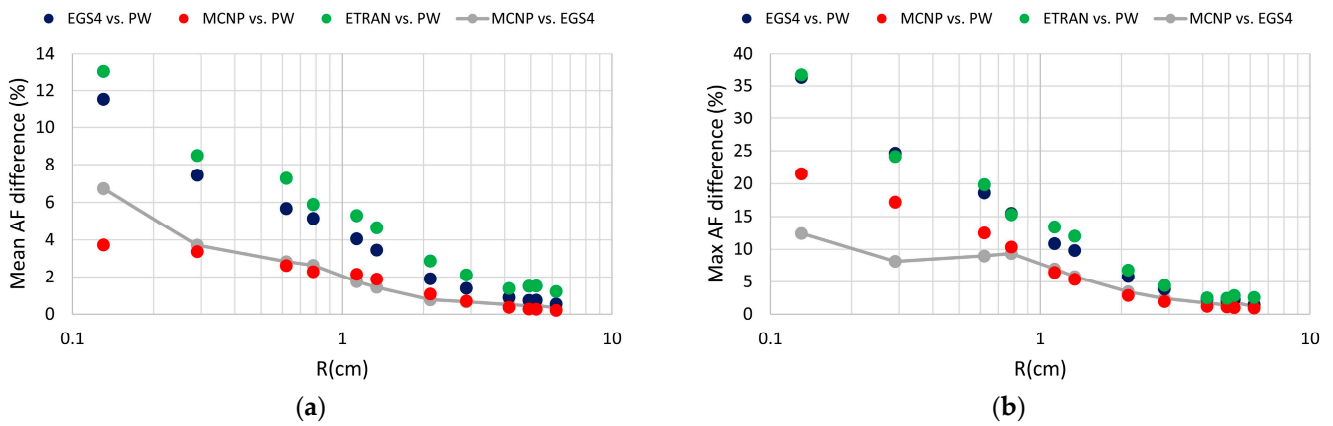


Figure 6. The mean (panel a) and maximum (panel b) percentage difference of the absorbed fraction (AF) values between the MC data and the results of the present work (PW), for the examined electron energies (100 keV–4 MeV) and for different sphere radii (1.3 mm–6.2 cm). For comparison, the (mean and maximum) differences between the MCNP and EGS4 codes are also included.

3.3. S Factor

The S factor is calculated from the absorbed fraction using Equation (2). In Figure 7, we present the S factor difference, $100 \frac{(S_{PW} - S_{MIRDcell})}{S_{MIRDcell}}$, between the analytic calculations of the present work (PW) and the MIRDcell software for monoenergetic electrons in the energy range 1 keV–4 MeV and various sphere radii (10, 50, 100, 500, 1000, 5000 μm).

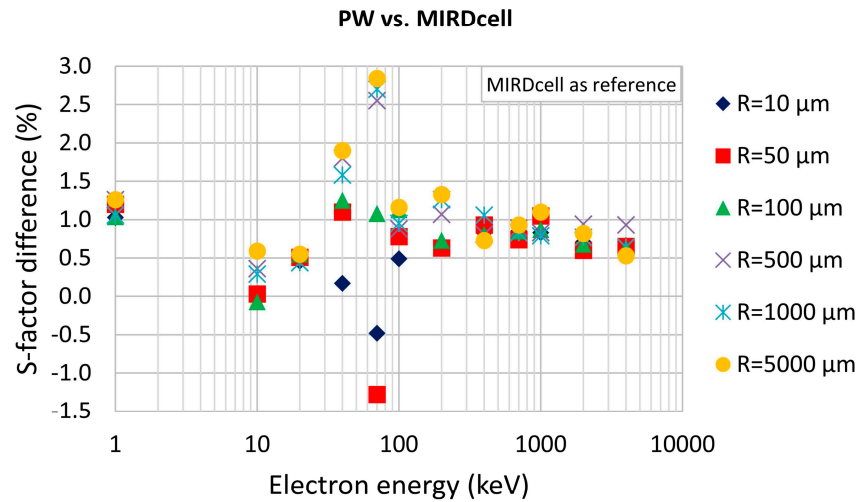


Figure 7. Percentage difference of S factor between the analytic calculations of the present work (PW) and the MIRDcell Software for electron energies in the range 1 keV–4 MeV and different sphere radius (R).

3.4. Geant4 Monte Carlo Calculations

3.4.1. Effect of Step Length (SL)

The sensitivity of the Geant4 S factor calculations on the choice of the step-length (SL) parameter in the simulations is examined in Figures 8 and 9. Specifically, the S factors calculated by the convolution integral using the analytic relations of the present work (PW) are compared against Geant4 (version 10.5) simulations for three SL parameters (SL = default, SL = R, SL = R/10) and three target spheres (R = 0.1 mm, R = 1 mm, and R = 5 mm). The default Step Length is 1 mm for energies up to about 400 keV and varies from 1.2 to 5.6 mm for the energy range of 400 keV to 4 MeV according to the stepping function [46]. Unless otherwise stated, the Geant4 Standard Option 4 EM model is used in the simulations. In these simulations, the tracking and the production cut-off energies

were set at 100 eV, because this value is generally considered as the lowest energy limit of validity of Geant4 (see Section 2.4).

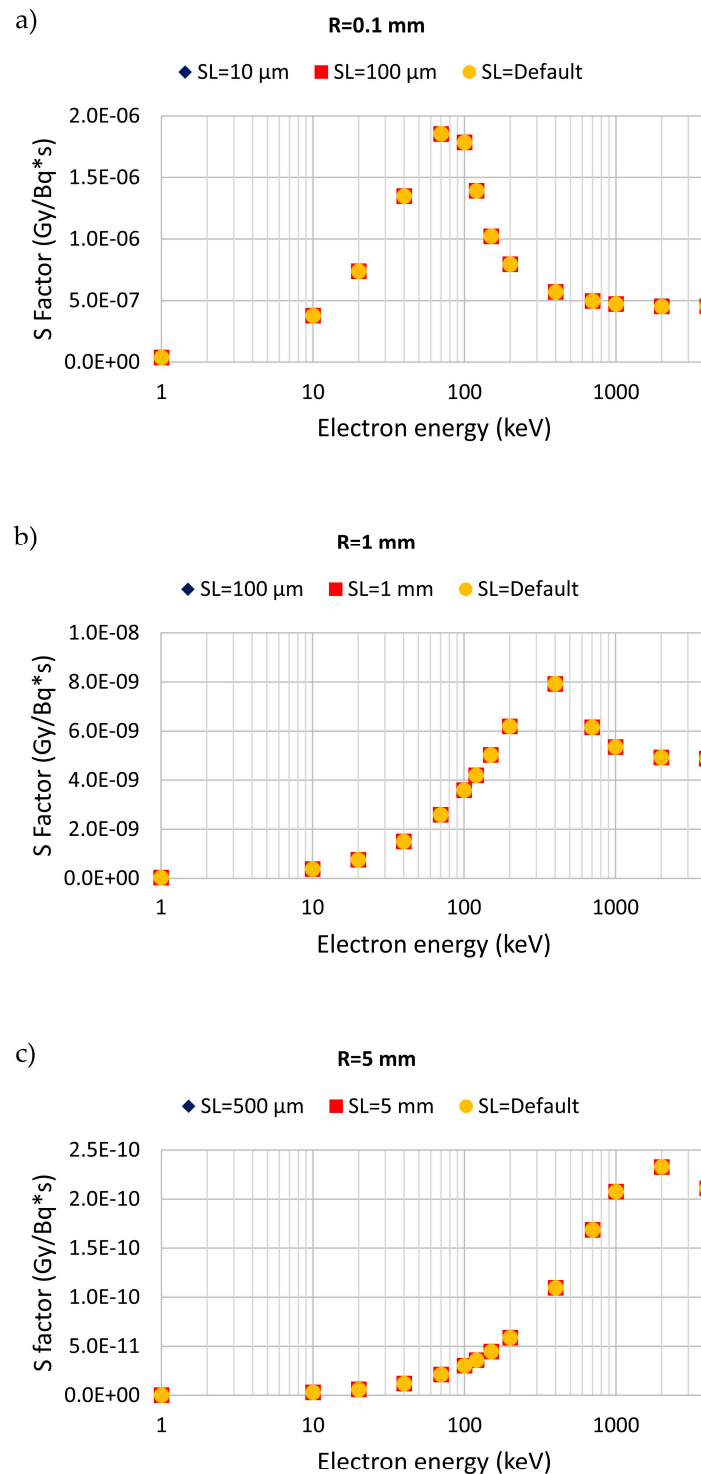


Figure 8. Geant4 calculated S factor values for spheres of radius $R = 0.1$ mm (panel a), $R = 1$ mm (panel b), and $R = 5$ mm (panel c) as a function of electron energy for different choices of the Step Length (SL) parameter. The tracking and production cut-off energies are set at 100 eV in these simulations.

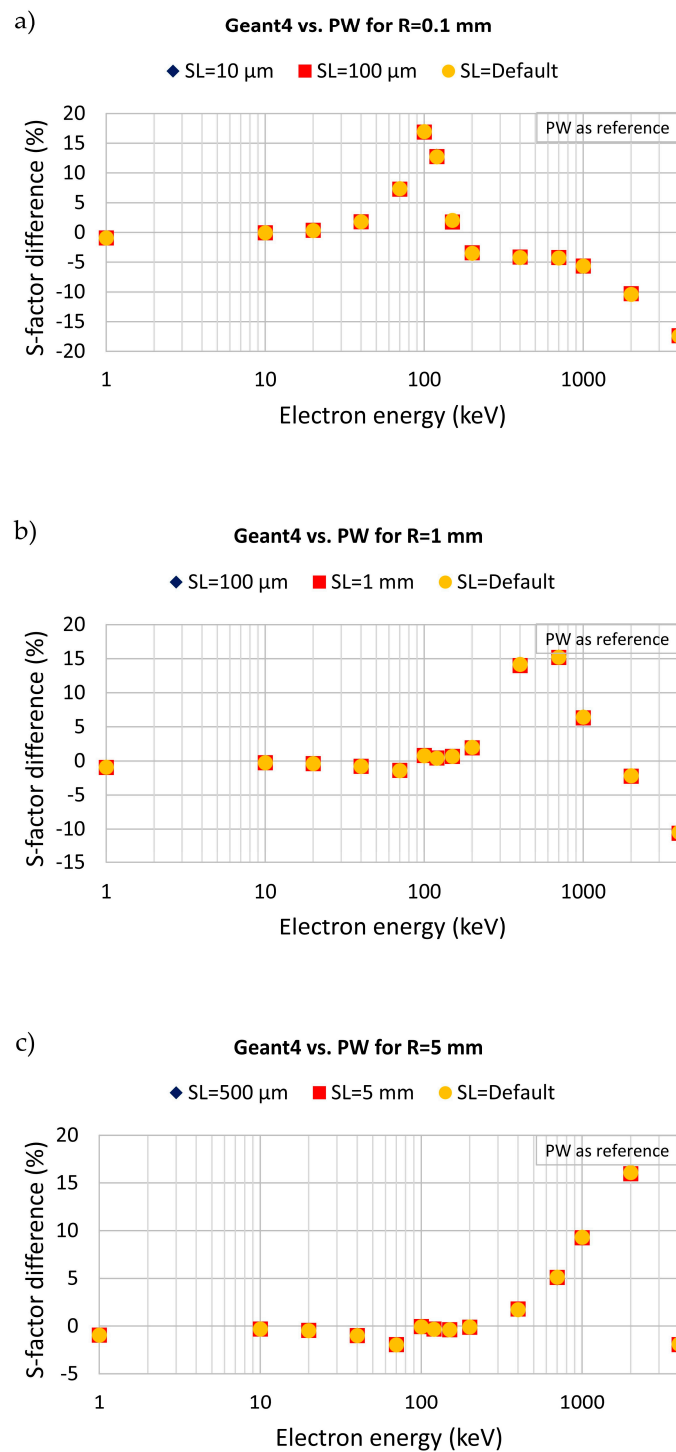


Figure 9. Percentage difference of S factor between the analytic results of the present work (PW) and the Geant4 simulations for different Step Length (SL) parameters as a function of the electron energy for spheres of radius $R = 0.1$ mm (panel a), $R = 1$ mm (panel b), and $R = 5$ mm (panel c). The tracking and production cut-off energies are set at 100 eV in these simulations.

In Figure 9 (panels a to c), we present the S factor difference, $100 \frac{(S_{\text{Geant4}} - S_{\text{PW}})}{S_{\text{PW}}}$, between the Geant4 simulations (with different SL parameters) and the analytic calculations of the present work (PW) for monoenergetic electrons in the energy range 1 keV–4 MeV and different sphere radii ($R = 0.1$ mm, $R = 1$ mm, and $R = 5$ mm).

3.4.2. Effect of Cut-Off Energy (CE)

The sensitivity of the Geant4 S factor calculations on the choice of CE used in the simulations is examined in Figure 10. Specifically, the S factor difference, $100 \frac{(S_{\text{Geant4}} - S_{\text{PW}})}{S_{\text{PW}}}$, between the analytic calculations of the present work (PW) and the Geant4 (version 10.5) simulations, for three CE values (CE = 100 eV, CE = 250 eV, and CE = 1 keV) and three target spheres (R = 0.1, R = 1, and R = 5 mm), is presented. In these simulations, we have set the SL at the default value.

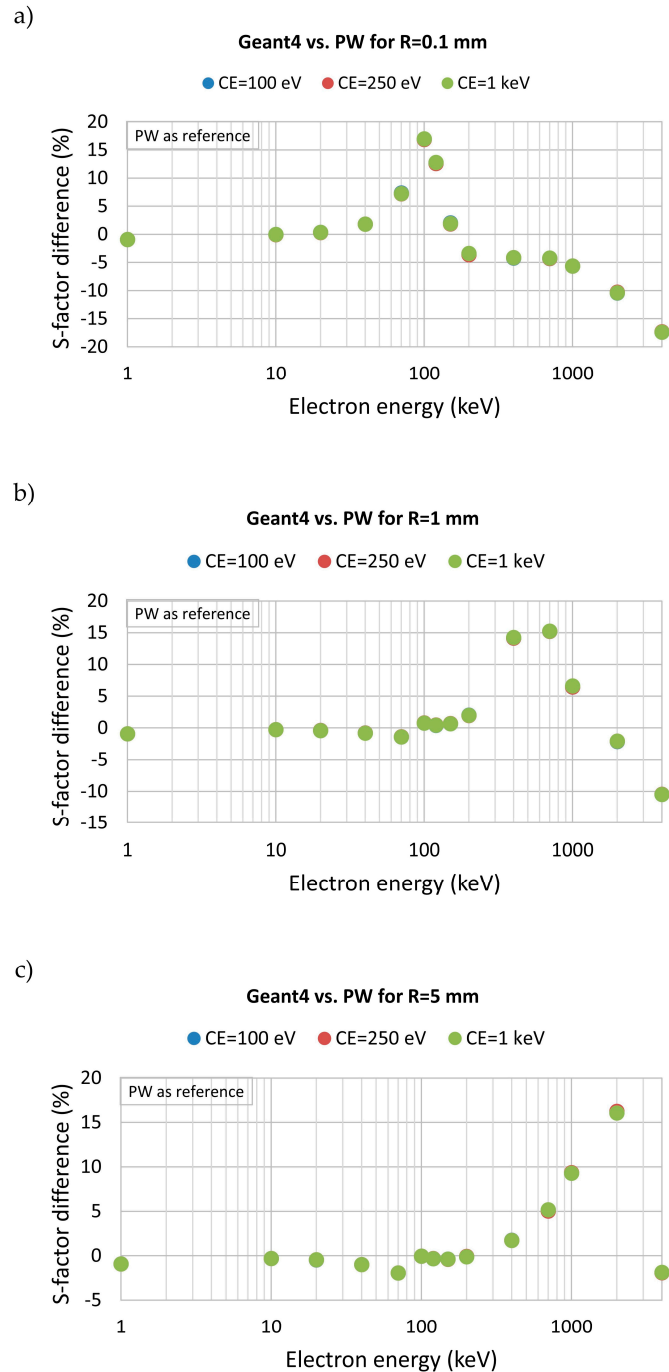


Figure 10. Percentage difference of S factor between the analytic calculations of the present work (PW) and the Geant4 simulations for different CE as a function of electron energy, and for spheres of radius R = 0.1 mm (panel a), R = 1 mm (panel b), and R = 5 mm (panel c). In these simulations, we have set SL = default.

3.4.3. Effect of Geant4 Ionization Model

The sensitivity of the Geant4 S factor calculations on the choice of the ionization model used in the simulations is examined in Figure 11. Specifically, we present the S factor difference, $100 \frac{(S_{\text{LowEnergy}} - S_{\text{Standard}})}{S_{\text{Standard}}}$, between the low-energy EM ionization models (Livermore, Penelope) and the Standard EM ionization model, for the three target spheres (R = 0.1 mm, R = 1 mm, and R = 5 mm). In these simulations, we have set SL = default and CE = 100 eV.

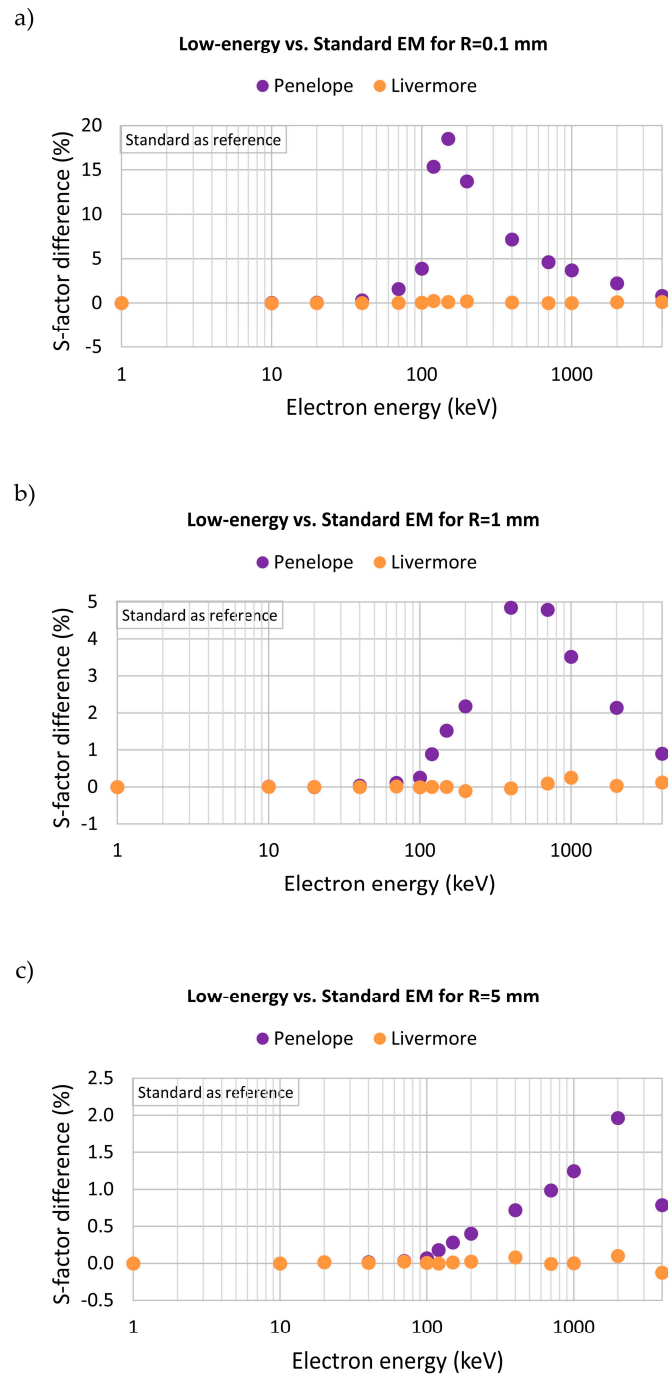


Figure 11. Percentage difference of S factor between the Low-energy EM ionization models (Livermore, Penelope) and the Standard EM ionization model of Geant4 as a function of electron energy for spheres of radius R = 0.1 mm (panel a), R = 1 mm (panel b), and R = 5 mm (panel c). In these simulations, we have set SL = default and CE = 100 eV.

4. Discussion

As can be seen from Figure 3, the new range–energy relations (Equations (14)–(16)) offer an almost excellent representation (within 1.5%) of Cole’s numerical data in the 100 keV–20 MeV energy range, while they are also in good agreement (within 5%) from ICRU Report 90 data (see Figure 4). Thus, the present range–energy relations together with the Cole–Howell relations at lower energies, allow for DPK-based calculations of the absorbed fraction (and S factor) by the convolution integral (Equation (4)) over a very broad energy interval (20 eV–20 MeV), which covers most applications of radiotherapeutic interest. The application of the new relations to the case of intermediate-size target volumes relevant to micrometastasis and disseminated disease is investigated in subsequent figures. Specifically, in Figures 5 and 6, we compare the present calculations against published MC data, which cover sphere radii between 1.3 mm and 6.2 cm and electron energies from 100 keV to 4 MeV. For mm-size spheres (radius 1.3–7.8 mm), the present calculations exhibit larger differences against EGS4, ETRAN, Geant4, and MCNPX and smaller for MCNP. Specifically, when averaged over the electron energies examined (100 keV–4 MeV), the maximum differences vary between 15 and 37% for ETRAN, 15 and 36% for EGS4, and 10 and 21% for MCNP. In terms of Geant4 and MCNPX codes, the maximum differences for the available presented data are 16–23% for Geant4 and 14% for MCNPX. Interestingly, the maximum differences between EGS4 and MCNP are comparable (9–12%). In all cases, differences decrease with increasing electron energy. On the other hand, for the cm-sized spheres, the differences between the present calculations and the MC data steadily decrease for all MC codes. Specifically, when averaged over the electron energies examined (100 keV–4 MeV), the maximum differences vary between 3 and 13% for ETRAN, 1 and 11% for EGS4, 1 and 6% for MCNP, 3 and 7% for Geant4, and 0.5 and 2% for MCNPX. Note that for Geant4 and MCNPX, no data are available for some spheres and electron energies. Again, the maximum differences between EGS4 and MCNP are similar (1–7%). Thus, the differences between the present DPK-based calculations and the MC codes are comparable to the differences observed among the codes. However, although an overall good agreement is observed against the MC codes (on average better than ~10% in most cases), the present DPK-based calculations tend to consistently underestimate the MC-based absorbed fractions. The underestimation is higher for the smaller spheres (~mm radius) and at energies where the range of electrons is comparable to the size of the sphere. A possible explanation is that the present DPK-based calculations are based on a range–energy relation deduced from Cole’s experimental data that seem to overestimate the penetration depth of electrons, as they resemble, instead, the CSDA range of ICRU (see Figure 2). In turn, the use of the CSDA range (instead of the penetration depth) in the convolution integral, Equation (4), will underestimate the actual energy deposition in the target by allowing electrons to travel and deposit energy further away. This underestimation is smaller as the size of the sphere is increasing (or the primary electron energy is decreasing), because of significant self-absorption within the target sphere.

In Figure 7, the present S factor calculations are compared against the MIRDcell Software, which adopts a similar DPK-based approach, for spheres of radius from 10 μ m to 5 mm. The maximum difference between the present calculations and MIRDcell is less than 3%, regardless of the sphere size. It is worth pointing out the excellent agreement (within 1.5%) between the present results and MIRDcell for energies higher than 100 keV (and for all spheres), whereby our new range–energy relations apply.

In the second part of this study, we compare S factor results for spheres of radius equal to 0.1 mm, 1 mm, and 5 mm based on the present DPK-based calculations against the Geant4 simulations carried out in this work. Specifically, in Figures 8–10, we study the influence of changing the simulation parameters available in the Geant4 toolkit, such as the step length (SL) and the tracking and production cut-off energies (CE). For all spheres, the differences between the Geant4 simulations and the DPK-based calculations are up to 20% irrespective of the choice of the SL and CE parameters. For all spheres, the difference in the S factor gradually increases with electron energy and becomes largest at the energy

where the range of electrons is comparable to the size of the sphere, i.e., at 100 keV for the 0.1 mm sphere, 700 keV for the 1 mm sphere, and 2 MeV for the 5 mm sphere. The underestimations of the present S factor calculations compared to Geant4 are consistent with the observation made above in relation to the other MC codes; that is, for most of the energy range investigated, the present DPK-based approach predicts lower energy deposition (see discussion in relation to Figure 5). However, at even higher energies, the DPK-based calculations become higher compared to the Geant4-based S factor. This trend is already seen against the other MC codes for the mm-sized volumes (see $R = 1.3, 2.9, 6.2,$ and 7.8 mm in Figure 5). This observation may be explained by the fact that the DPK-based approach is based on the assumption of a continuous energy-loss rate, which neglects the production and transport of delta-rays. At sufficiently high energies, these delta rays are energetic enough so that they can leave the target volume, thus depositing part of their energy outside. So, it may be reasoned that, at sufficiently high energies and/or small volumes, the DPK-based approach should overestimate the MC-based S factors that explicitly consider the delta-ray escape from the volume.

Finally, the dependence of Geant4-based S factors on the ionization model used in the simulations is shown in Figure 11. It can be seen that the influence of the ionization model is sensitive to the size of the target volume. Specifically, whereas the difference between the Standard and Livermore models is negligible for all energies and target volumes, the Penelope model results in higher S factor values by up to 20% for the 0.1 mm sphere, 5% for the 1 mm sphere, and 2% for the 1 mm sphere. These maximum differences are observed at electron energies that correspond to penetration ranges comparable to target dimensions. As already mentioned, this situation is very sensitive to the details of electron transport in terms of physics models and transport methodology.

5. Conclusions

In this study, we have presented new range–energy analytic expressions, effective for electrons from 100 keV to 20 MeV, which, together with the Cole–Howell relations at lower energies, facilitate DPK-based calculations of the absorbed fraction and S factor over a broad electron energy range (20 eV–20 MeV), covering most applications of radiotherapeutic interest. DPK-based calculations of self-absorbed fractions and S factors for intermediate-size target volumes (~mm to cm), relevant to micrometastasis and disseminated disease, are in excellent agreement (within 1.5%) with the MIRDcell software, while also being in fair agreement (within 10–20%) with published MC data as well as with new Geant4 simulations at energies up to 4 MeV. With respect to the Geant4-based S factor calculations, the choice (within reasonable limits) of step-size and tracking/production cut-off energies seems inconsequential for this range of target spheres, whereas the choice of the ionization model may need some caution when mm-size targets are considered.

Author Contributions: Conceptualization, D.E. and I.K.; methodology, C.K., I.K. and D.E.; software, C.K., I.K., V.I. and S.I.; validation, C.K. and I.K.; formal analysis, C.K., I.K., and D.E.; investigation, C.K. and I.K.; resources, I.K., S.I. and D.E.; data curation, C.K. and I.K.; writing—original draft preparation, C.K.; writing—review and editing, C.K., I.K., V.I., S.I. and D.E.; supervision, I.K. and D.E.; project administration, D.E. All authors have read and agreed to the published version of the manuscript.

Funding: This research received no external funding.

Institutional Review Board Statement: Not applicable.

Informed Consent Statement: Not applicable.

Data Availability Statement: The raw data supporting the conclusions of this article will be made available by the authors on request.

Conflicts of Interest: The authors declare no conflicts of interest.

References

1. Sgouros, G.; Bolch, W.E.; Chiti, A.; Dewaraja, Y.K.; Emfietzoglou, D.; Hobbs, R.F.; Konijnenberg, M.; Sjögren-Gleisner, K.; Strigari, L.; Yen, T.-C.; et al. ICRU REPORT 96, Dosimetry-Guided Radiopharmaceutical Therapy. *J. ICRU* **2021**, *21*, 1–212. [[CrossRef](#)]
2. Sgouros, G.; Bodei, L.; McDevitt, M.R.; Nedrow, J.R. Radiopharmaceutical Therapy in Cancer: Clinical Advances and Challenges. *Nat. Rev. Drug Discov.* **2020**, *19*, 589–608. [[CrossRef](#)] [[PubMed](#)]
3. St. James, S.; Bednarz, B.; Benedict, S.; Buchsbaum, J.C.; Dewaraja, Y.; Frey, E.; Hobbs, R.; Grudzinski, J.; Roncali, E.; Sgouros, G.; et al. Current Status of Radiopharmaceutical Therapy. *Int. J. Radiat. Oncol. Biol. Phys.* **2021**, *109*, 891–901. [[CrossRef](#)] [[PubMed](#)]
4. Stokke, C.; Kvassheim, M.; Blakkisrud, J. Radionuclides for Targeted Therapy: Physical Properties. *Molecules* **2022**, *27*, 5429. [[CrossRef](#)]
5. Bardiès, M.; Myers, M.J. Computational Methods in Radionuclide Dosimetry. *Phys. Med. Biol.* **1996**, *41*, 1941–1955. [[CrossRef](#)] [[PubMed](#)]
6. Brownell, G.L.; Ellett, W.H.; Reddy, A.R. MIRDO Pamphlet No. 3: Absorbed Fractions for Photon Dosimetry. *J. Nucl. Med. Off. Publ. Soc. Nucl. Med.* **1968**, *9* (Suppl. S1), 27–39.
7. Snyder, W.S. MIRDO Pamphlet No. 5: Estimates of Absorbed Fractions for Monoenergetic Photon Sources Uniformly Distributed in Various Organs of a Heterogeneous Phantom. *J. Nucl. Med.* **1969**, *10*, 1.
8. Ellett, W.H.; Humes, R.M. MIRDO Pamphlet No. 8: Absorbed Fractions for Small Volumes Containing Photon-Emitting Radioactivity. *J. Nucl. Med.* **1971**, *12* (Suppl. S5), 25–32.
9. Snyder, W.; Ford, G.; Warner, G.; Watson, S. MIRDO Pamphlet No. 11: S, Absorbed Dose per Unit Cumulated Activity for Selected Radionuclides and Organs. *Soc. Nucl. Medicine* **1975**.
10. Coffey, J.L.; Cristy, M.; Warner, G.G. MIRDO Pamphlet No. 13: Specific Absorbed Fractions for Photon Sources Uniformly Distributed in the Heart Chambers and Heart Wall of a Heterogeneous Phantom. *J. Nucl. Med.* **1981**, *22*, 65–71.
11. Bouchet, L.G.; Bolch, W.E.; Weber, D.A.; Atkins, H.L.; Poston, J.W. MIRDO Pamphlet No. 15: Radionuclide S Values in a Revised Dosimetric Model of the Adult Head and Brain. *J. Nucl. Med.* **1999**, *40*, 62S–101S.
12. Bolch, W.E.; Bouchet, L.G.; Robertson, J.S.; Wessels, B.W.; Siegel, J.A.; Howell, R.W.; Erdi, A.K.; Aydogan, B.; Costes, S.; Watson, E.E. MIRDO Pamphlet No. 17: The Dosimetry of Nonuniform Activity Distributions—Radionuclide S Values at the Voxel Level. *J. Nucl. Med.* **1999**, *40*, 11S–36S. [[PubMed](#)]
13. Bouchet, L.G.; Bolch, W.E.; Blanco, H.P.; Wessels, B.W.; Siegel, J.A.; Rajon, D.A.; Clairand, I.; Sgouros, G. MIRDO Pamphlet No. 19: Absorbed Fractions and Radionuclide S Values for Six Age-Dependent Multiregion Models of the Kidney. *J. Nucl. Med.* **2003**, *44*, 1113–1147. [[PubMed](#)]
14. Berger, M.J. *Improved Point Kernels for Electron and Beta-Ray Dosimetry*; National Bureau of Standards: Gaithersburg, MD, USA, 1973.
15. Simpkin, D.J.; Mackie, T.R. EGS4 Monte Carlo Determination of the Beta Dose Kernel in Water. *Med. Phys.* **1990**, *17*, 179–186. [[CrossRef](#)]
16. Ferrer, L.; Chouin, N.; Bitar, A.; Lisbona, A.; Bardiès, M. Implementing Dosimetry in GATE: Dose-Point Kernel Validation with GEANT4 4.8.1. *Cancer Biother. Radiopharm.* **2007**, *22*, 125–129. [[CrossRef](#)]
17. Seltzer, S.M. Electron-Photon Monte Carlo Calculations: The ETRAN Code. *Int. J. Radiat. Appl. Instrum. Part A Appl. Radiat. Isot.* **1991**, *42*, 917–941. [[CrossRef](#)]
18. Kawrakow, I. The EGSnrc Code System, Monte Carlo Simulation of Electron and Photon Transport. *NRCC Rep. Pirs-701* **2001**.
19. Briesmeister, J.F. MCNP-A General Monte Carlo Code for Neutron and Photon Transport. In *LA-7396-M 3A*; Los Alamos National Laboratory: Los Alamos, NM, USA, 1986.
20. Agostinelli, S.; Allison, J.; Amako, K.; Apostolakis, J.; Araujo, H.; Arce, P.; Asai, M.; Axen, D.; Banerjee, S.; Barrand, G.; et al. Geant4—A Simulation Toolkit. *Nucl. Instrum. Methods Phys. Res. Sect. A Accel. Spectrometers Detect. Assoc. Equip.* **2003**, *506*, 250–303. [[CrossRef](#)]
21. Bolch, W.E.; Kim, E.-H. Calculations of Electron Single Event Distributions for Use in Internal Beta Microdosimetry. *Radiat. Prot. Dosim.* **1994**, *52*, 77–80. [[CrossRef](#)]
22. Nikjoo, H.; Martin, R.F.; Charlton, D.E.; Terrissol, M.; Kandaiya, S.; Lobachevsky, P. Modelling of Auger-Induced DNA Damage by Incorporated ¹²⁵I. *Acta Oncol.* **1996**, *35*, 849–856. [[CrossRef](#)] [[PubMed](#)]
23. Torres-García, E.; Garnica-Garza, H.M.; Ferro-Flores, G. Monte Carlo Microdosimetry of ¹⁸⁸Re- and ¹³¹I-Labelled Anti-CD20. *Phys. Med. Biol.* **2006**, *51*, N349–N356. [[CrossRef](#)]
24. Emfietzoglou, D.; Kostarelos, K.; Hadjidakis, P.; Bousis, C.; Fotopoulos, A.; Pathak, A.; Nikjoo, H. Subcellular S-Factors for Low-Energy Electrons: A Comparison of Monte Carlo Simulations and Continuous-Slowing-down Calculations. *Int. J. Radiat. Biol.* **2008**, *84*, 1034–1044. [[CrossRef](#)] [[PubMed](#)]
25. Šefl, M.; Incerti, S.; Papamichael, G.; Emfietzoglou, D. Calculation of Cellular S-Values Using Geant4-DNA: The Effect of Cell Geometry. *Appl. Radiat. Isot.* **2015**, *104*, 113–123. [[CrossRef](#)] [[PubMed](#)]
26. Nikjoo, H.; Emfietzoglou, D.; Liamsuwan, T.; Taleei, R.; Liljequist, D.; Uehara, S. Radiation Track, DNA Damage and Response—A Review. *Rep. Prog. Phys.* **2016**, *79*, 116601. [[CrossRef](#)] [[PubMed](#)]
27. Dingfelder, M.; Ritchie, R.H.; Turner, J.E.; Friedland, W.; Paretzke, H.G.; Hamm, R.N. Comparisons of Calculations with PARTRAC and NOREC: Transport of Electrons in Liquid Water. *Radiat. Res.* **2008**, *169*, 584–594. [[CrossRef](#)] [[PubMed](#)]

28. Incerti, S.; Kyriakou, I.; Bernal, M.A.; Bordage, M.C.; Francis, Z.; Guatelli, S.; Ivanchenko, V.; Karamitros, M.; Lampe, N.; Lee, S.B.; et al. Geant4-DNA Example Applications for Track Structure Simulations in Liquid Water: A Report from the Geant4-DNA Project. *Med. Phys.* **2018**, *45*, e722–e739. [[CrossRef](#)] [[PubMed](#)]
29. Bernal, M.A.; Bordage, M.C.; Brown, J.M.C.; Davidková, M.; Delage, E.; El Bitar, Z.; Enger, S.A.; Francis, Z.; Guatelli, S.; Ivanchenko, V.N.; et al. Track Structure Modeling in Liquid Water: A Review of the Geant4-DNA Very Low Energy Extension of the Geant4 Monte Carlo Simulation Toolkit. *Phys. Medica* **2015**, *31*, 861–874. [[CrossRef](#)] [[PubMed](#)]
30. Incerti, S.; Ivanchenko, A.; Karamitros, M.; Mantero, A.; Moretto, P.; Tran, H.N.; Mascialino, B.; Champion, C.; Ivanchenko, V.N.; Bernal, M.A.; et al. Comparison of GEANT4 Very Low Energy Cross Section Models with Experimental Data in Water. *Med. Phys.* **2010**, *37*, 4692–4708. [[CrossRef](#)] [[PubMed](#)]
31. Incerti, S.; Baldacchino, G.; Bernal, M.; Capra, R.; Champion, C.; Francis, Z.; Guèye, P.; Mantero, A.; Mascialino, B.; Moretto, P.; et al. The GEANT4-DNA Project. *Int. J. Model. Simul. Sci. Comput.* **2010**, *01*, 157–178. [[CrossRef](#)]
32. Kyriakou, I.; Sakata, D.; Tran, H.N.; Perrot, Y.; Shin, W.-G.; Lampe, N.; Zein, S.; Bordage, M.C.; Guatelli, S.; Villagrasa, C.; et al. Review of the Geant4-DNA Simulation Toolkit for Radiobiological Applications at the Cellular and DNA Level. *Cancers* **2021**, *14*, 35. [[CrossRef](#)]
33. Berger, M.J. MIRD Pamphlet No. 2: Energy Deposition in Water by Photons from Point Isotropic Sources. *J. Nucl. Med.* **1968**, *9* (Suppl. S1), 15–25.
34. Berger, M.J. MIRD Pamphlet No. 7: Distribution of Absorbed Dose around Point Sources of Electrons and Beta Particles in Water and Other Media. *J. Nucl. Med.* **1971**, *12* (Suppl. S5), 5–23.
35. Berger, M.J. Beta-Ray Dosimetry Calculations with the Use of Point Kernels. In *Radiation Dose and Effects*; United States Atomic Energy Commission: Washington, DC, USA, 1970; pp. 63–86.
36. Siegel, J.A.; Stabin, M.G. Absorbed Fractions for Electrons and Beta Particles in Spheres of Various Sizes. *J. Nucl. Med.* **1994**, *35*, 152–156. [[PubMed](#)]
37. Stabin, M.G.; Konijnenberg, M.W. Re-Evaluation of Absorbed Fractions for Photons and Electrons in Spheres of Various Sizes. *J. Nucl. Med.* **2000**, *41*, 149–160. [[PubMed](#)]
38. Amato, E.; Lizio, D.; Baldari, S. Absorbed Fractions for Electrons in Ellipsoidal Volumes. *Phys. Med. Biol.* **2011**, *56*, 357–365. [[CrossRef](#)] [[PubMed](#)]
39. Olguin, E.; President, B.; Ghaly, M.; Frey, E.; Sgouros, G.; Bolch, W.E. Specific Absorbed Fractions and Radionuclide S-Values for Tumors of Varying Size and Composition. *Phys. Med. Biol.* **2020**, *65*, 235015. [[CrossRef](#)] [[PubMed](#)]
40. Stabin, M. Nuclear Medicine Dosimetry. *Phys. Med. Biol.* **2006**, *51*, R187–R202. [[CrossRef](#)] [[PubMed](#)]
41. Goddu, S.M.; Budinger, T.F. (Eds.) *MIRD Cellular S. Values: Self-Absorbed Dose per Unit Cumulated Activity for Selected Radionuclides and Monoenergetic Electron and Alpha Particle Emitters Incorporated into Different Cell Compartments*; Society of Nuclear Medicine: Reston, VA, USA, 2003; ISBN 978-0-932004-46-8.
42. Cole, A. Absorption of 20-eV to 50,000-eV Electron Beams in Air and Plastic. *Radiat. Res.* **1969**, *38*, 7. [[CrossRef](#)] [[PubMed](#)]
43. Howell, R.W.; Rao, D.V.; Sastry, K.S.R. Macroscopic Dosimetry for Radioimmunotherapy: Nonuniform Activity Distributions in Solid Tumors. *Med. Phys.* **1989**, *16*, 66–74. [[CrossRef](#)]
44. Vaziri, B.; Wu, H.; Dhawan, A.P.; Du, P.; Howell, R.W. In collaboration with the SNMMI MIRD Committee: MIRD Pamphlet No. 25: MIRDcell V2.0 Software Tool for Dosimetric Analysis of Biologic Response of Multicellular Populations. *J. Nucl. Med.* **2014**, *55*, 1557–1564. [[CrossRef](#)]
45. Goddu, S.M.; Howell, R.W.; Rao, D.V. Cellular Dosimetry: Absorbed Fractions for Monoenergetic Electron and Alpha Particle Sources and S-Values for Radionuclides Uniformly Distributed in Different Cell Compartments. *J. Nucl. Med.* **1994**, *35*, 303–316.
46. Apostolakis, J.; Asai, M.; Bogdanov, A.G.; Burkhardt, H.; Cosmo, G.; Elles, S.; Folger, G.; Grichine, V.M.; Gumplinger, P.; Heikkinen, A.; et al. Geometry and Physics of the Geant4 Toolkit for High and Medium Energy Applications. *Radiat. Phys. Chem.* **2009**, *78*, 859–873. [[CrossRef](#)]
47. Allison, J.; Amako, K.; Apostolakis, J.; Arce, P.; Asai, M.; Aso, T.; Bagli, E.; Bagulya, A.; Banerjee, S.; Barrand, G.; et al. Recent Developments in Geant4. *Nucl. Instrum. Methods Phys. Res. Sect. A Accel. Spectrometers Detect. Assoc. Equip.* **2016**, *835*, 186–225. [[CrossRef](#)]
48. Allison, J.; Amako, K.; Apostolakis, J.; Araujo, H.; Arce Dubois, P.; Asai, M.; Barrand, G.; Capra, R.; Chauvie, S.; Chytracsek, R.; et al. Geant4 Developments and Applications. *IEEE Trans. Nucl. Sci.* **2006**, *53*, 270–278. [[CrossRef](#)]
49. Chetty, I.J.; Curran, B.; Cygler, J.E.; DeMarco, J.J.; Ezzell, G.; Faddegon, B.A.; Kawrakow, I.; Keall, P.J.; Liu, H.; Ma, C.-M.C.; et al. Report of the AAPM Task Group No. 105: Issues Associated with Clinical Implementation of Monte Carlo-based Photon and Electron External Beam Treatment Planning. *Med. Phys.* **2007**, *34*, 4818–4853. [[CrossRef](#)] [[PubMed](#)]
50. Chauvie, S.; Guatelli, S.; Ivanchenko, V.; Longo, F.; Mantero, A.; Mascialino, B.; Nieminen, P.; Pandola, L.; Parlati, S.; Peralta, L.; et al. Geant4 Low Energy Electromagnetic Physics. In *Proceedings of the IEEE Symposium Conference Record Nuclear Science 2004, Rome, Italy, 16–22 October 2004*; IEEE: Rome, Italy, 2004; Volume 3, pp. 1881–1885.
51. Kyriakou, I.; Ivanchenko, V.; Sakata, D.; Bordage, M.C.; Guatelli, S.; Incerti, S.; Emfietzoglou, D. Influence of Track Structure and Condensed History Physics Models of Geant4 to Nanoscale Electron Transport in Liquid Water. *Phys. Medica* **2019**, *58*, 149–154. [[CrossRef](#)]
52. Cullen, D.E.; Hubbell, J.H.; Kissel, L. *EPDL97: The Evaluated Photo Data Library97 Version*; Lawrence Livermore National Lab. (LLNL): Livermore, CA, USA, 1997.

53. Perkins, S.T.; Cullen, D.E.; Chen, M.H.; Rathkopf, J.; Scofield, J.; Hubbell, J.H. *Tables and Graphs of Atomic Subshell and Relaxation Data Derived from the LLNL Evaluated Atomic Data Library (EADL), Z = 1–100*; Lawrence Livermore National Lab. (LLNL): Livermore, CA, USA, 1991.
54. Perkins, S.T.; Cullen, D.E.; Seltzer, S.M. Tables and Graphs of Electron-Interaction Cross-Sections from 10 eV to 100 GeV Derived from the LLNL Evaluated Electron Data Library (EEDL), Z = 1–100. *UCRL-50400* **1991**, *31*, 21–24.
55. Ivanchenko, V.N.; Kadri, O.; Maire, M.; Urban, L. Geant4 Models for Simulation of Multiple Scattering. *J. Phys. Conf. Ser.* **2010**, *219*, 032045. [[CrossRef](#)]
56. Kyriakou, I.; Emfietzoglou, D.; Ivanchenko, V.; Bordage, M.C.; Guatelli, S.; Lazarakis, P.; Tran, H.N.; Incerti, S. Microdosimetry of Electrons in Liquid Water Using the Low-Energy Models of Geant4. *J. Appl. Phys.* **2017**, *122*, 024303. [[CrossRef](#)]
57. Salvat, F.; Fernández-Varea, J.M.; Sempau, J. PENELOPE-2006: A Code System for Monte Carlo Simulation of Electron and Photon Transport. In *Workshop Proceedings*; Nuclear Energy Agency, Organization for Economic Co-operation and Development: Barcelona, Spain, 2006; Volume 4, p. 7.
58. Liljequist, D. A Simple Calculation of Inelastic Mean Free Path and Stopping Power for 50 eV–50 keV Electrons in Solids. *J. Phys. D Appl. Phys.* **1983**, *16*, 1567–1582. [[CrossRef](#)]
59. Kadri, O.; Ivanchenko, V.; Gharbi, F.; Trabelsi, A. Incorporation of the Goudsmit–Saunderson Electron Transport Theory in the Geant4 Monte Carlo Code. *Nucl. Instrum. Methods Phys. Res. Sect. B Beam Interact. Mater. At.* **2009**, *267*, 3624–3632. [[CrossRef](#)]
60. ICRU REPORT 90 Key Data for Ionizing-Radiation Dosimetry: Measurement Standards and Applications. *J. ICRU* **2014**, *14*, 1–110. [[CrossRef](#)] [[PubMed](#)]

Disclaimer/Publisher’s Note: The statements, opinions and data contained in all publications are solely those of the individual author(s) and contributor(s) and not of MDPI and/or the editor(s). MDPI and/or the editor(s) disclaim responsibility for any injury to people or property resulting from any ideas, methods, instructions or products referred to in the content.